Data-driven exploration of swarmalators with second-order harmonics

R. Senthamizhan, R. Gopal,* and V. K. Chandrasekar†
Department of Physics, Centre for Nonlinear Science and Engineering, School of Electrical and Electronics Engineering, SASTRA Deemed University, Thanjavur 613 401, India

(Received 31 December 2023; accepted 2 May 2024; published 6 June 2024)

We explore the dynamics of a swarmalator population comprising second-order harmonics in phase interaction. A key observation in our study is the emergence of the active asynchronous state in swarmalators with second-order harmonics, mirroring findings in the one-dimensional analog of the model, accompanied by the formation of clustered states. Particularly, we observe a transition from the static asynchronous state to the active phase wave state via the active asynchronous state. We have successfully delineated and quantified the stability boundary of the active asynchronous state through a completely data-driven method. This was achieved by utilizing the enhanced image processing capabilities of convolutional neural networks, specifically, the U-Net architecture. Complementing this data-driven analysis, our study also incorporates an analytical stability of the clustered states, providing a multifaceted perspective on the system's behavior. Our investigation not only sheds light on the nuanced behavior of swarmalators under second-order harmonics, but also demonstrates the efficacy of convolutional neural networks in analyzing complex dynamical systems.

DOI: 10.1103/PhysRevE.109.064303

I. INTRODUCTION

Synchronization and swarming have been at the forefront of research initiatives to gain insight into the collective behavior of coupled systems [1]. Following Kuramoto's seminal work in 1975, synchronization studies sharply increased and have continued to rise ever since [2]. The influence of these investigations is so significant that its application is widely present in science and technology, ranging from power grid networks [3,4] to cardiac pacemaker cells [5,6], to name a few. Additionally, there are numerous examples of this in natural systems, such as the chorusing frogs, fireflies [7], clapping in unison [8], and crowd movements [9]. In parallel, the study of swarming behavior has also attracted the attention of researchers based on the Vicsek model of swarming of self-propelled agents influenced by the neighboring particles lying inside a unit radius [10], and this model focuses on the spatial position and structures of the particle clusters. In continuation, depending on the spatial movement of the particles, synchronization phenomena were studied by the introduction of mobile agents or moving oscillators [11,12]. These studies paid particular attention when looking at the movements of flocks of animals, flocks of birds, schools of fish, swarms of insects, etc. [13–16]. Discoveries from these studies have applications in technological fields such as swarm robotics, aerial drones, and even traffic control [17,18].

However, in recent times, synchronization and swarming have been explored together in the fascinating phenomenon of swarmalation, a common collective behavior seen in the entities called *swarmalators* [19]. This is mainly referred to as the "swarming" oscillators, denoting the mobile phase oscillators that can self-organize in time and swarm in space [20]. They currently describe the various systems where swarming and synchronization coexist and interact. For instance, Japanese tree frogs [21], magnetic domain walls [22], swarming robots [23], starfish embryos [24], and Janus particles [25] are a few examples where swarmalation effects are encountered.

Tanaka [26], and Iwasa and Tanaka [27] have carried out significant research that laid the platform for swarmalator systems while studying the movement and dynamics of chemotactic oscillators, which typically refers to the movement of an organism or entity in response to a chemical stimulus, suggesting that these oscillators respond to such stimuli in a dynamic and interconnected manner. Following this, the study by O'Keeffe *et al.* [28,29] introduced a three-dimensional mathematical model of swarmalators. These are characterized by their movement in a two-dimensional plane, and their dynamics are based on the Kuramoto oscillator, laying the pathway for a new branch of mobile oscillators. The study reports five long-term collective states that demonstrate a wide range of spatial aggregation and phase synchronization. These states are static sync, static phase wave, active phase wave, and splintered phase wave. In these states the spatial attraction between two swarmalators is influenced by their relative phase, and the phase coupling is affected by the spatial distance between them. Recently, a two-dimensional (2D) model comparable to the three-dimensional (3D) swarmalator model was also developed as described by O'Keeffe *et al.* [28]. This model is essentially a pair of analytically tractable Kuramoto-type models and has received well-deserved attention from the research community [28–35].

Significant efforts have been made during the last few years, and the dynamics of the swarmalators were further

*Corresponding author: gopalphysics@gmail.com
†Corresponding author: chandru25nld@gmail.com

studied for different interaction functions and coupling schemes by including external forcing [28–36,45]. The researchers are interested in delving deeper into the study of such systems due to the discovery of many new collective states. Even though traditional approaches such as analytical and numerical methods enable understanding of diverse properties of such swarmalator systems, some properties still need to be understood to identify the dynamical transitions of the collective states. Even so, research in the fascinating world of the swarmalator model is still in its early stages, with ample scope for further exploration.

Therefore, we extended the swarmalator model by introducing second-order modes in the phase interaction function, similar to the model introduced by Smith's recent work [37] reporting the stability, bifurcation, and structural properties of stationary clustered states. Our study, in contrast, mainly focuses on the distinct collective dynamics of active states in the swarmalators with second-order harmonic phase coupling. This type of coupling is interesting because it can result in certain dynamical features such as cluster synchrony and more [38], which is already seen in physical systems such as photochemical, electrochemical, and genetic oscillators [39,40].

In this study we first consider second-order harmonics in the swarmalators model, and their complete collective dynamical states are explored. Second, we applied a machine-learning (ML) approach to investigate the system based on data-driven analysis and determine the classification of collective dynamical states arising from the dynamics of swarmalators. With growing interest in ML, recent works on physical systems and the Kuromoto model have demonstrated successful progress by adapting the appropriate ML approach to underlying facts of chaotic behaviors and providing so-called model-free prediction of the behavior of dynamical systems [41,42]. Along with recent advances in ML algorithms for phase transition in the Kuramoto model, it is significant to consider the synchronization transition using the ML approach [43]. As a model for describing phase oscillators that swarm around space, they synchronize in time and are also a suitable candidate for the platform to deal with the ML approach. Despite the rich properties of these kinds of models, the applications of ML approaches on this system still need to be worked out.

Our present study examines the swarmalator model using data-driven approaches to distinguish between several collective dynamical states. We have adopted the ML approach of convolutional neural networks, specifically employing the U-Net neural network model, a type of convolutional neural network for identifying certain dynamical states such as the active asynchronous state, active phase wave, and splintered phase wave, and for determining the critical boundaries among them [44].

The paper is organized as follows. After the present introduction in Sec. I, we present in Sec. II the model under study. In Sec. III the order parameter employed in the present study and the occurrence of different collective dynamical states are described. Meanwhile, Sec. IV focuses on an approximation of the critical boundary of an active asynchronous state by using the semantic segmentation capability of U-Net. Section V is devoted to the conclusion.

II. MODEL AND SIMULATION

We give a model for swarmalators whose phase and spatial dynamics are coupled and represented as follows [19,21,22,28,45]:

$$\dot{\mathbf{x}}_i = v_i + \frac{1}{N}\sum_{j\neq i}^{N}[\chi_{\text{att}}(\mathbf{x}_j - \mathbf{x}_i)\tau(\theta_j - \theta_i) - \chi_{\text{rep}}(\mathbf{x}_j - \mathbf{x}_i)], \tag{1}$$

$$\dot{\theta}_i = \omega_i + \frac{K}{N}\sum_{j\neq i}^{N}\tau_{\text{att}}(\theta_j - \theta_i)\chi(\mathbf{x}_j - \mathbf{x}_i), \tag{2}$$

with $i, j = 1, ..., N$. For our case of two spatial dimensions, the position of the ith swarmalator is denoted by $\mathbf{x}_i = (x_i, y_i)$, and θ_i is the internal phase of each swarmalator, where $\chi_{\text{att}}(\mathbf{x}_j - \mathbf{x}_i)$ and $\chi_{\text{rep}}(\mathbf{x}_j - \mathbf{x}_i)$ are the attractive and repulsive interaction terms, respectively. $\tau(\theta_j - \theta_i)$ is the phase interaction function, which describes the influence of the difference in phase between the ith and jth swarmalators on their movement. $\tau_{\text{att}}(\theta_j - \theta_i)$ is the phase interaction function and $\chi(\mathbf{x}_j - \mathbf{x}_i)$ is the spatial interaction function, which describes the influence of the distance between the ith and jth swarmalators on their phases.

Consider the following model where spatial interaction functions are based on power law with positive exponents $\epsilon_1, \epsilon_2, \epsilon_3$ along with a Kuramoto-inspired phase interaction function with higher-order harmonic h:

$$\dot{\mathbf{x}}_i = v_i + \frac{1}{N}\left[\sum_{j\neq i}^{N}\frac{\mathbf{x}_j - \mathbf{x}_i}{|\mathbf{x}_j - \mathbf{x}_i|^{\epsilon_1}}[A + J\cos(\theta_j - \theta_i)] - B\frac{\mathbf{x}_j - \mathbf{x}_i}{|\mathbf{x}_j - \mathbf{x}_i|^{\epsilon_2}}\right], \tag{3}$$

$$\dot{\theta}_i = \omega_i + \frac{K}{N}\sum_{j\neq i}^{N}\frac{\sin[h(\theta_j - \theta_i)]}{|\mathbf{x}_j - \mathbf{x}_i|^{\epsilon_3}}. \tag{4}$$

The natural frequency and self-propulsion velocity of the ith swarmalator are denoted by ω_i and v_i, respectively. The interaction strengths of the phase and spatial dynamics in $\dot{\theta}_i$ and $\dot{\mathbf{x}}_i$ are denoted by K and J, respectively. A is selected such that $\forall J \in [-A, +A]$, $A + J\cos(\theta_j - \theta_i) > 0$, which ensures $\tau(\theta_j - \theta_i)$ is always positive, contributing to the spatial attraction, and B is the spatial repulsion strength. The exponents $\epsilon_1 = 1$ and $\epsilon_2 = 2$ play a crucial role in enabling swarming behavior. The condition $1 \leqslant \epsilon_1 < \epsilon_2$ ensures that the repulsion force dominates the attraction force locally among the swarmalators. By having $\epsilon_2 = 2$ we achieve short-range repulsion, where the strength of repulsion decreases as the distance between swarmalators increases, following an inverse square law. This means that the swarmalators will tend to move away from each other when they are in proximity. On the other hand, having $\epsilon_1 = 1$ ensures long-range attraction. Since the exponent in the denominator is smaller than ϵ_2, there is an attractive force that acts over longer distances. This implies that swarmalators are inclined to move closer to one another, even when they are at greater distances. In addition to these exponents, ϵ_3 is chosen to be the value one

to ensure that neighboring swarmalators' influence on their phases resembles spatial attraction. The chosen exponents are pivotal in ensuring that attractive force among the swarmalators remains constant, irrespective of their mutual distances, with the strength of interaction being exclusively phase dependent.

The numerical simulations were performed using a population of $N = 500$ swarmalators for $T = 1000$ time steps, with the parameters A and B set to 1. By the choice of reference frame, the natural frequency ω_i and self-propulsion velocity v_i were kept at 0. The initial positions of all the swarmalators were randomly distributed between–2 and +2 for both x and y coordinates. The initial phases were drawn randomly from a uniform distribution ranging from $-\pi$ to $+\pi$, and to study the effect of second-order harmonics, we set the order of harmonic h to 2 in Eq. (4). The values of interaction strengths (J, K) of phase and spatial coupling among the swarmalators, along with the second-order harmonics, determine the destiny of the swarmalator system, where we observe different collective states by varying the values of the interaction strength pair. Incorporating second-order harmonics within the swarmalator model leads to the emergence of distinct states such as the clustered π state (CPIS), mixed π state (MPIS), active phase wave (APW), splintered phase wave (SPPW), static asynchronous state (SAS), static phase wave (SPW), and active asynchronous state (AAS). Among these, the formation of the CPIS, MPIS, and AAS are directly attributable to the inclusion of second-order harmonics. However, swarmalators with distributed natural frequencies exhibit only two possible states: the active asynchronous state (AAS) and the static asynchronous state (SAS) as given in Appendix A. In the following sections we explore these dynamical states and define several order parameters that are useful for examining the properties of the emerging collective states.

III. RESULTS AND DISCUSSION

A. Order parameters

In the context of swarmalators with second-order harmonics, different order parameters have been utilized to separate distinct states based on their collective behavior. To distinguish the various states, we define a set of complex order parameters [19] as follows:

$$s_{1\pm} = \frac{1}{N}\sum_{j=1}^{N} e^{i(\phi_j \pm \theta_j)}, \tag{5}$$

$$s_{2\pm} = \frac{1}{N}\sum_{j=1}^{N} e^{i(\phi_j \pm 2\theta_j)}, \tag{6}$$

where $\phi_i = \tan^{-1}(\frac{y_i}{x_i})$ represents the spatial angle and θ_i denotes the phase of the ith swarmalators, respectively. Here N is the total number of swarmalators in the system. We designate s_1 as the $\min(s_{1+}, s_{1-})$. s_1 approaching unity indicates the full correlation between spatial and phase angles, whereas a null value of s_1 signifies the absence of correlation. In a similar vein, s_2, defined as $\min(s_{2+}, s_{2-})$, captures the essence of synchronization among swarmalators that exhibit a phase difference of π. For distinguishing a splintered phase wave from an active phase wave, γ is defined and is given by

$$\gamma = \frac{N_{\text{rotation}}}{N}, \tag{7}$$

where N_{rotation} is the number of oscillators that executes at least one full rotation in spatial angle $\phi = \tan^{-1}(\frac{y}{x})$.

B. Clustering and static states

Incorporating second-order harmonics into the phase interaction yields two clustered states: the clustered π state (CPIS) and the mixed π state (MPIS). These clustered π states have been previously identified in a solvable model of swarmalators [46]. The phase locking of swarmalators characterizes these π states with a phase difference of π, and they showcase radial symmetry and static characteristics. To elaborate, for a given phase ψ ranging from 0 to 2π, the swarmalators' phases are locked in such a way that for a subset of them, denoted as $[\theta_1, \theta_2, ..., \theta_p]$, all phases equal ψ. For the remaining swarmalators, indicated by $[\theta_{p+1}, \theta_{p+2}, ..., \theta_N]$, the phases are set at $\psi + \pi$. Here, p represents the number of swarmalators at phase ψ. When the condition $K > 0$ is achieved, these π states gain stability. This stability criterion for π states using a reduced system is discussed in Appendix B, and the π states differentiate further for different values of J. The CPIS is observed when $J > 0$, illustrated in Fig. 1(a), where swarmalators with identical phases are grouped into two distinct clusters separated by a phase difference of π. In contrast, for $J \leqslant 0$ the MPIS becomes evident as depicted in Fig. 1(b), where two populations of swarmalators maintain a π phase difference but are randomly scattered in space, forming a disklike structure without any movement. The distinction of various dynamical states is made with the help of order parameters and is depicted in Fig. 2.

To clarify the distinction between the mixed π state (MPIS) and the clustered π state (CPIS), we rely on the order parameter s_1. Both the MPIS and CPIS states form two clusters offset by a π phase difference. However, the CPIS is characterized by its phase-cohesive clusters in the XY plane, meaning swarmalators with like phases form clusters. Contrastingly, in the MPIS, swarmalators are interspersed within a circular region, showing no regard for phase congruity. A high s_1 value, close to 1, points to the well-organized CPIS state, whereas a lower s_1 value, near zero, suggests the less orderly MPIS state, presented in Fig. 2(b).

Considering the values of $K = 0$ for $J > 0$, we can see static states are characterized by the static phase wave (SPW) as shown in Fig. 1(e), where swarmalators exhibit a fixed phase within a continuous ringlike formation, and the static asynchronous state (SAS), depicted in Fig. 1(g), marked by a lack of phase alignment that results in total desynchronization and absence of motion. To examine the behavior of the SAS state apart from the MPIS state, we also use the order parameter s_2, and it is plotted in Fig. 2(d). In the SAS, swarmalators show no pattern in how their spatial positions relate to their phases, leading to an s_2 value that is nearly zero. In contrast, the MPIS state tends for swarmalators to cluster by phase, pushing the s_2 value higher than in the SAS state.

Furthermore, the SPW state is identified using another order parameter s_{2+}, illustrated in Fig. 2(e), where the occur-

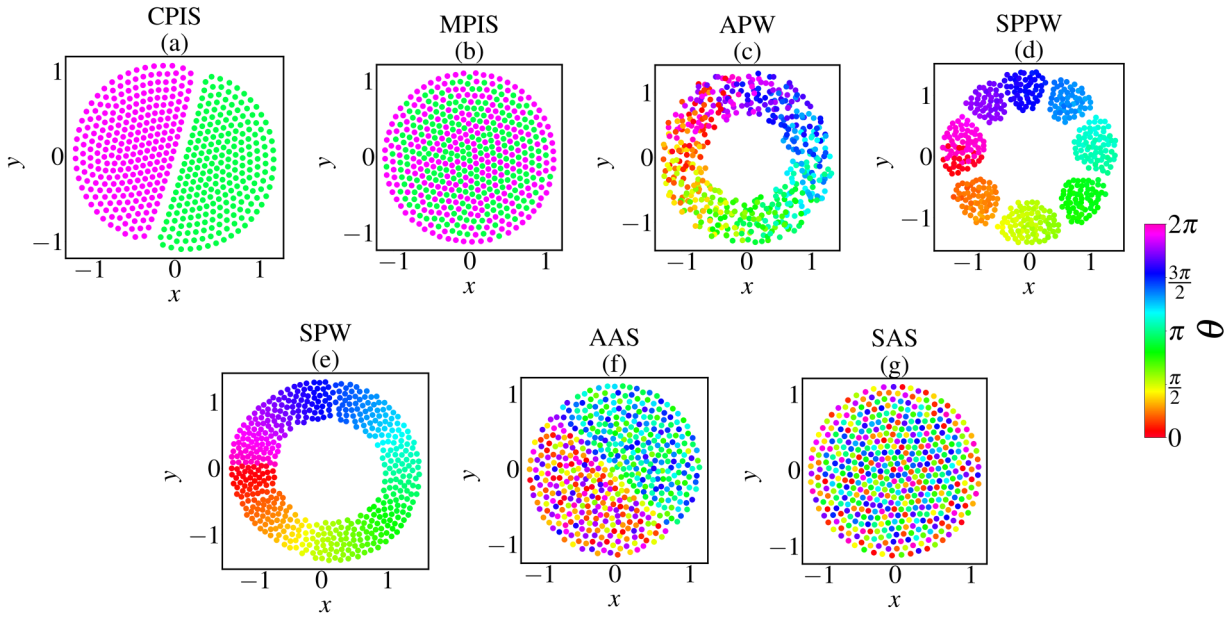

FIG. 1. Spatial plot of swarmalators in which their phases are depicted in different colors. The plot shows seven distinct states, obtained by varying the interaction strengths J and K: (a) clustered π state (CPIS), for $J = 0.1$ and $K = 1$; (b) mixed π state (MPIS), for $J = -0.1$ and $K = 0.1$; (c) active phase wave (APW), for $J = 1.0$ and $K = -0.75$; (d) splintered phase wave (SPPW), for $J = 1.0$ and $K = -0.1$; (e) static phase wave (SPW), for $J = 1.0$ and $K = 0.0$; (f) active asynchronous state (AAS), for $J = 0.1$ and $K = -1$; and (g) static asynchronous state (SAS), for $J = -0.1$ and $K = -0.75$.

rence of a peak at $K = 0$ indicates SPW. In the SPW there exists a direct correlation where the spatial angle ϕ_i is equal to the phase angle θ_i plus a constant C. This results in a stronger correlation between ϕ and θ than what is observed in adjacent states.

C. Active states

Further, when $K < 0$ and $J > 0$, an APW, SPPW, and AAS exist. The SPPW [Fig. 1(d)] features swarmalators segregated into different groups, each with distinct phases with movement confined within their group. The active phase wave APW

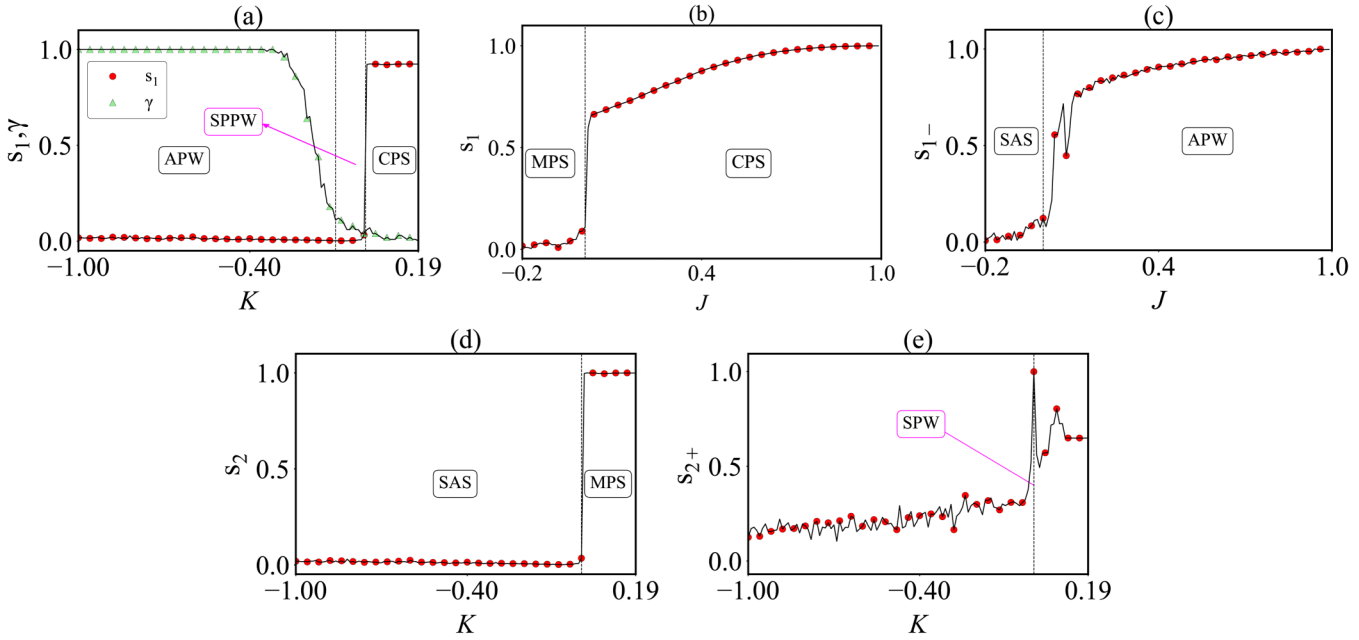

FIG. 2. Order parameter shows state transitions with respect to interaction strengths J and K. (a) In the s_1, γ vs K plot for $J = 0.5$, s_1 clarifies the transitions between APW, SPPW, and CPIS while γ separates APW and SPPW. (b) The s_1 vs J graph for $K = 0.1$ distinguishes MPIS from CPIS. (c) In the s_{1-} vs J plot at $K = -0.8$, we observe clear separation among SAS and APW. (d) The s_2 vs K curve for $J = -0.2$, with $s_2 = \min(s_{2+}, s_{2-})$, serves to differentiate SAS from MPIS. (e) Finally, the s_{2+} vs K plot for $J = 0.5$ effectively distinguishes SPW from adjacent states.

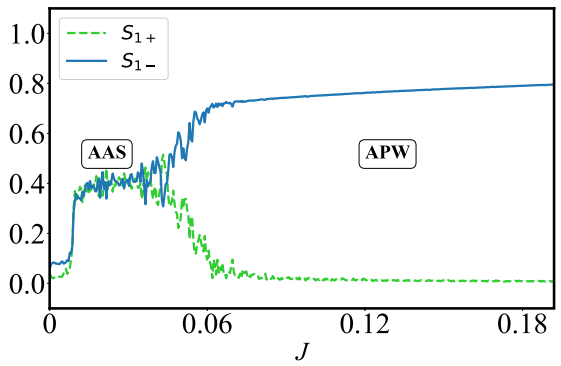

FIG. 3. s_{1+} and s_{1-} vs J for $K = -0.6$, showing the fluctuating order parameter in the AAS region.

involves spatially counter-rotating swarmalators forming an annular structure as shown in Fig. 1(c). A crucial distinction within the study of swarmalators is separating the CPIS from the different dynamics of the APW and the SPPW. The CPIS is characterized by a highly synchronized phase configuration in which two distinct clusters are set apart by a phase difference of π. This high synchronization within the CPIS is captured by the order parameter s_1, depicted in Fig. 3(a), typically approaching unity. Conversely, the APW and SPPW are differentiated by a more complex distribution of phases among the swarmalators and a notable lack of synchronization, reflected by an s_1 value approaching zero.

The APW and SPPW are analyzed using the order parameter γ shown in Fig. 2(a) to further differentiate. The SPPW is marked by limited movement within clusters, rarely completing a full spatial rotation. Hence γ is near zero. In contrast, the APW is characterized by swarmalators that move in a consistent circular trajectory, which translates to a γ close to 1.

The SAS, another distinct state, does not exhibit the dynamism of the APW. It is discerned from the APW through the order parameter s_{1-}, as illustrated in Fig. 2(c). Swarmalators in the SAS are relatively immobile, displaying no consistent relationship between their phase and spatial position, leading to s_{1-} values nearing zero. On the other hand, the APW demonstrates an active state where a certain degree of phase-position correlation exists, resulting in nonzero s_{1-} values indicative of the ongoing activity.

D. Active asynchronous state

An AAS was previously reported in one-dimensional (1D) analog of the model by O'Keeffe *et al.* [29] and Lizárraga *et al.* [47]. In AAS [Fig. 1(f)], swarmalators form a uniform disk in the XY plane rather than the annular structure seen in the APW. Each swarmalator undergoes continuous positional changes within the radial disk. From s_{1+} and s_{1-} as depicted in Fig. 3, it is evident that AAS exhibits some degree of phase-space order. However, s_{1+} and s_{1-} display irregular fluctuations in the active asynchronous state, indicating residual local ordering that briefly persists and generates the fluctuations. Furthermore, AAS exhibits partial phase-space order, and the phase θ vs spatial angle ϕ behavior in Fig. 4 highlights the critical difference between AAS and

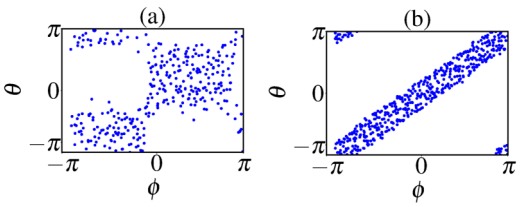

FIG. 4. (a) Spatial angle ϕ vs phase θ for AAS and (b) ϕ vs θ for APW, shows that the ϕ and θ are more correlated in APW relative to AAS.

APW, with a spatial angle more strongly correlated to phase in APW.

Additionally, in contrast to the static asynchronous state, AAS has velocities associated with each swarmalator. The instantaneous mean speed $v_{i,t}$ of the ith swarmalators at time t can be calculated as [48]

$$v_{i,t} = \sqrt{\left(\frac{\Delta x_{i,t}}{\Delta t}\right)^2 + \left(\frac{\Delta y_{i,t}}{\Delta t}\right)^2}. \tag{8}$$

Here, $\Delta x_{i,t}$ and $\Delta y_{i,t}$ denote the changes in the x and y coordinates of the ith swarmalators, respectively, between two consecutive time points $(t-1)$ and t. The speed vs time is plotted in Fig. 5, and it highlights the difference between AAS and static asynchronous state.

As illustrated in Fig. 3, no sharp transition is evident between AAS and APW. Since both are active states and exhibit chaotic behavior [49], the system becomes analytically intractable. Given that the determination of stability by the

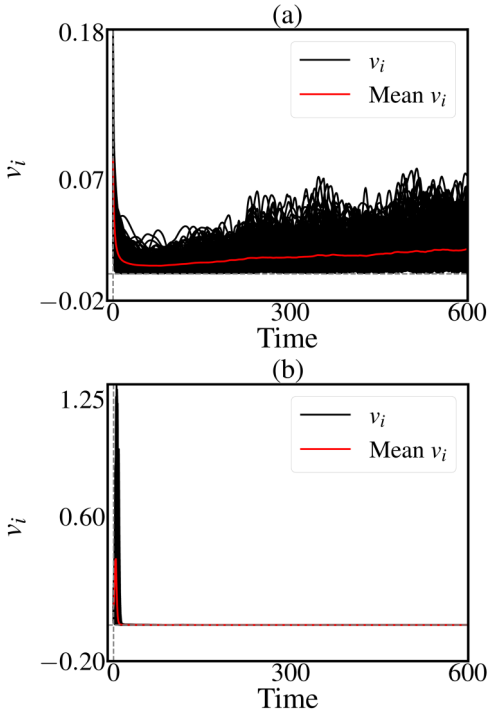

FIG. 5. Instantaneous mean speed vs time plot for (a) active asynchronous state obtained from $J = 0.1$ and $K = -1$ and (b) static asynchronous state for $J = -0.1$ and $K = -0.75$. v_i is the instantaneous mean speed of the swarmalators where $i = 0, 1, 2, ..., N$.

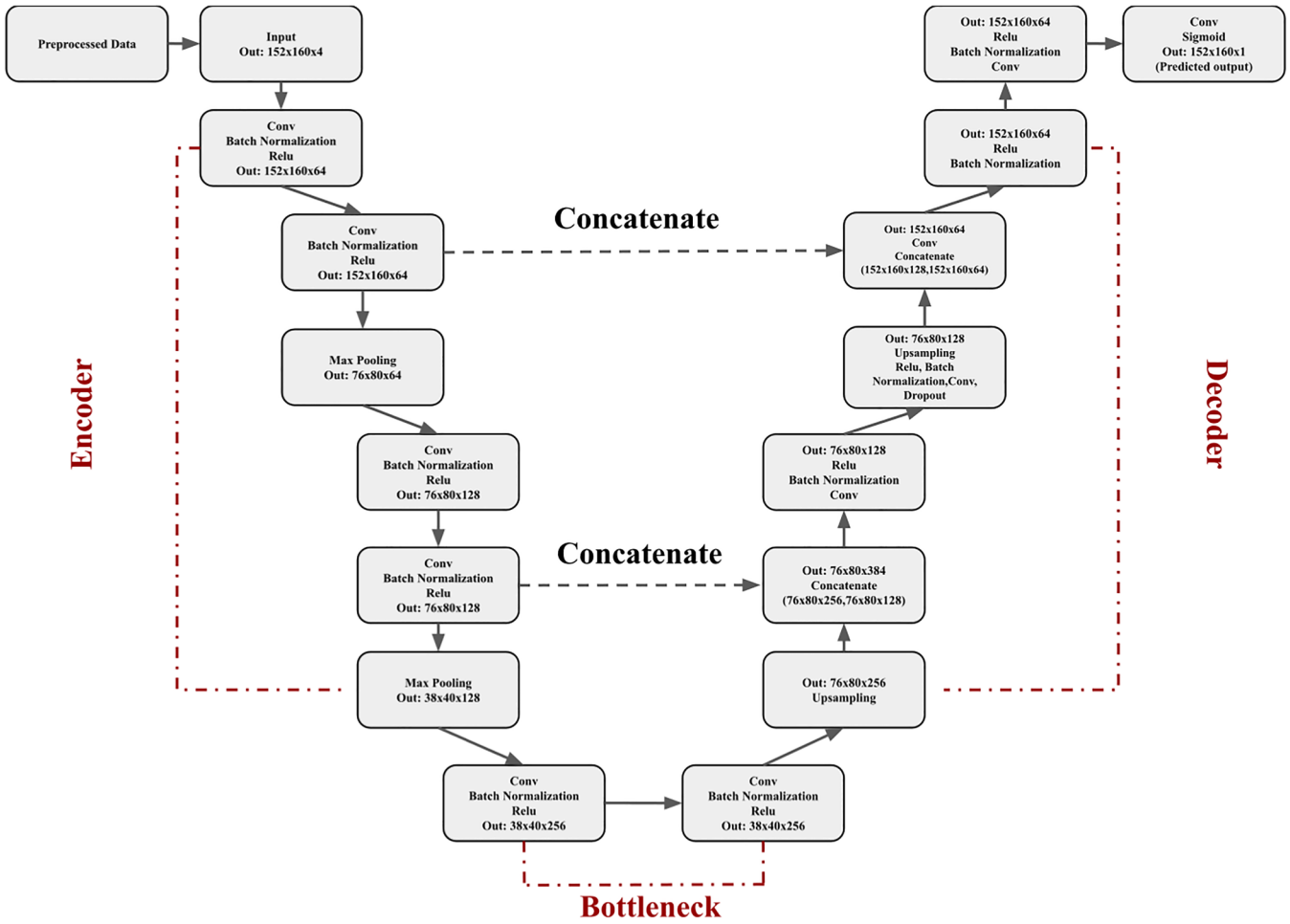

FIG. 6. U-Net network architecture.

order parameter yields only a less accurate approximation and the analytical approach is difficult to realize, we can leverage neural networks to identify the critical boundary for AAS. The emergent behaviors of swarmalators lend themselves well to data-driven techniques, as there are a number of features we can extract from the simulation data. By training classifiers on simulation data over a range of parameters, it is possible to delineate phase boundaries and characterize transitions between dynamical states.

IV. STABILITY APPROXIMATION OF AAS WITH DATA-DRIVEN TECHNIQUES

In the previous section we examined the dynamical states of our model under various parameters. Building upon this foundation, our study introduces a method to identify the stability line of AAS, employing the U-Net image segmentation neural network [50,51]. The primary application of the U-Net architecture lies in the domain of semantic segmentation. This process involves the partitioning of an image into several segments or regions. The objective is to distinguish and isolate objects within the image through a systematic labeling approach. In this scheme each label corresponds to a specific type or class of object. Initially developed for biomedical image segmentation [52], U-Net's versatile design has since been adapted for tasks including image classification, localization, and generation. A key advantage of U-Net is its ability to train efficiently on smaller datasets while retaining high speed and accuracy, a feature particularly valuable in the medical domain where labeled data is often scarce. This efficiency makes U-Net an ideal choice for classifying dynamical states in the parameter space, where extensive training data is limited.

A. U-Net network description

The model comprises two primary pathways: the contracting pathway, or "encoder," and the expanding pathway, or "decoder," as illustrated in Fig. 6. The encoder consists of successive convolutional layers with ReLU activation function and max pooling layers with pool size 2×2. In U-Net and similar deep-learning models, images are input as tensors [53]. For instance, an RGB image is represented as a tensor with dimensions corresponding to its height, width, and color channels. The convolution layers in our model are designed to take four-dimensional tensor inputs; therefore, the dataset, denoted as $\chi_{i,k}$, must be converted accordingly before being processed by these layers. The transformation is expressed as $\chi'_{i,j,k,l} = \chi_{i,k}$, where i, j, k, l represent the batch size, height of the tensor, width of the tensor, and number of channels, respectively. The output of a convolutional layer is

given by [54]

$$O_{ij} = \sum_m \sum_n \kappa_{mn} * \iota_{i+m,j+n} + \beta, \tag{9}$$

where κ_{mn} is the kernel matrix with height m and width n, $\iota_{i+m,j+n}$ is the part of the input feature map covered by the kernel, and β is the bias. The feature map is then fed into an activation function. The activation function used is the rectified linear unit (ReLU), defined as follows [55]:

$$\mathrm{ReLU}(O_{ij}) = \begin{cases} O_{ij}, & \text{if } O_{ij} > 0 \\ 0, & \text{if } O_{ij} \leqslant 0. \end{cases} \tag{10}$$

ReLU activation function introduces nonlinearity to the model. This nonlinearity is crucial for enabling the network to establish complex decision boundaries. The feature maps are then subjected to a max pooling layer. Here, they are downsampled, reducing their spatial dimensions while retaining the essential extracted features. This downsampling process effectively reduces the computational burden, thus enhancing the network's efficiency. This contracting path is akin to the feed-forward layers in other convolutional neural networks (CNNs), which reduces the spatial resolution of the input. The final layer of the encoder acts as a bottleneck, feeding the feature maps into the expansion layer. On the other hand, the expansion pathway or decoder is composed of successive layers where max pooling operators are replaced by upsampling operators, thus increasing the spatial resolution of the output. At each level of the expansive path, the feature map from the corresponding level of the contracting path is concatenated (skip connections) with the upsampled feature map. This process reintroduces the high-resolution features from the contracting path, which assists in better localization and detailed reconstruction in the final segmented image. Since our task involves binary classification, we have utilized binary cross entropy as the loss function. This choice is justified as it performs well with binary classes, even when they are imbalanced [56]. Additionally, each convolutional layer is equipped with L2 regularization, which adds a penalty to the loss function, thereby preventing overfitting and aiding in the model's generalization. The loss function, along with the regularization term, is expressed as [57]

$$L(\Upsilon, \hat{\Upsilon}) = -\frac{1}{\eta} \sum_{i=1}^{\eta} [\Upsilon_i \log(\hat{\Upsilon}_i) + (1 - \Upsilon_i) \log(1 - \hat{\Upsilon}_i)] + L_2, \tag{11}$$

$$L_2 = \lambda \sum_{i,j,k,c} W_{i,j,k,c}^2. \tag{12}$$

Υ represents the actual labels of the training samples, $\hat{\Upsilon}$ represents the predicted probabilities corresponding to the actual labels, and η is the number of samples. λ is the regularization parameter which controls the extent of regularization. A higher value of λ means more emphasis on keeping the weights small. $W_{i,j,k,c}$ represents the weights in the neural network model. The indices i, j, k, c refer to different dimensions in a convolutional neural network, such as width, height, depth, and channels. At the decoder's end, the output from the final convolutional layer is passed through a sigmoid activation function to obtain probability values. The sigmoid function, denoted as $\sigma(O_{ij})$, is defined for any real input O_{ij} as follows:

$$\sigma(O_{ij}) = \frac{1}{1 + e^{-O_{ij}}}. \tag{13}$$

The function σ maps any real-valued number into a value between 0 and 1, making it particularly useful for models where the output needs to be interpreted as a probability.

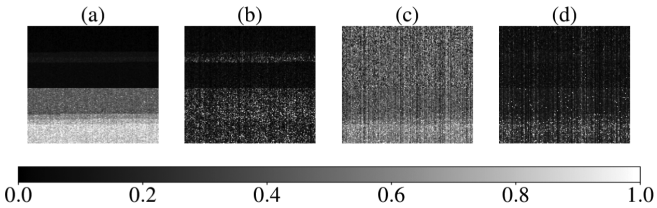

FIG. 7. Preprocessed training data of extracted statistical quantities after augmentation and reshaping. (a) Spread of PSD, (b) instantaneous deviation from the time average, (c) skewness, and (d) kurtosis.

B. Data preprocess and training

U-Net, designed explicitly for image segmentation, demands preprocessed data to match its structural requirements, which involves augmentation and reshaping of data. To achieve this, we utilized four statistical metrics: the spread of power spectral density (PSD), instantaneous deviation from the time average, kurtosis, and skewness. Each metric acts as a distinct channel, analogous to the RGB channels in an image. These channels are derived from the instantaneous mean speed time series of swarmalators, across various J and K values. We compiled a training dataset from a dense array of J and K values, producing multiple stripes of data points with diverse intervals in the range $-1 < K < 0$ and $1 > J > 0$. This ensures that the training data consists of data points that belong to both AAS and APW states. The corresponding labels for this data were generated manually based on the J and K values they obtained. Each input feature was normalized and transformed into a 152×160 matrix through reshaping and duplication for augmentation, shown in Fig. 7. These four channels were then combined into a tensor with dimensions of $152 \times 160 \times 4$. We extracted a training set ($121 \times 160 \times 4$) and a validation set ($31 \times 160 \times 4$), each expanding to $152 \times 160 \times 4$ through augmentation to meet the network's input criteria. We set the batch size to 8 for training and limited epochs to 50, based on various trials, to avoid overfitting. After the 50th epoch, U-Net displayed a training loss of 0.7359 and an accuracy of 1.00, alongside a validation loss of 1.0891 and an accuracy of 0.8947. With the increase in epoch, there is no observable increment in the validation accuracy, even with the reduced loss. This suggests the model has reached its learning capacity and is thereby ready to predict the unseen data.

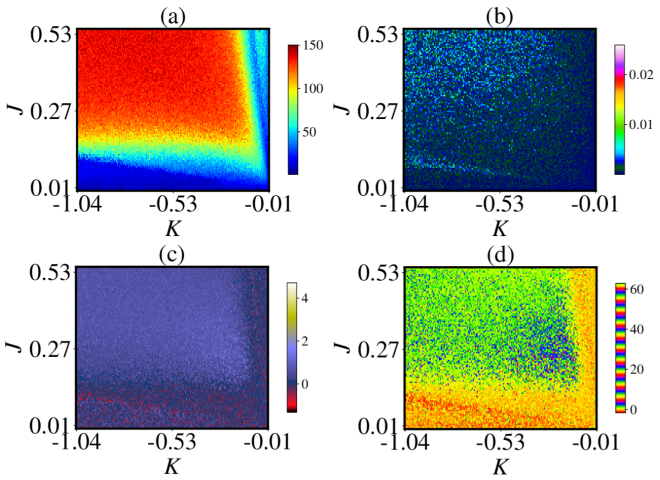

FIG. 8. Color maps show the statistical measures extracted from the time series of instantaneous average of velocities in the JK plane: (a) spread of PSD, (b) instantaneous deviation from the time average, (c) skewness, and (d) kurtosis.

C. Prediction and postprocessing

For prediction, the channels used are same as the training data, which include spread, deviation, kurtosis, and skewness. These are calculated for a range of values, precisely, $0.01 < J < 0.5$ and $-1 < K < -0.01$. The data is then normalized and resized to dimensions of $152 \times 160 \times 4$ as shown in Fig. 8, using a min-max scaler which rescales data to a specified range, typically 0 to 1, ensuring consistent feature scales for optimal performance, and subsequently fed into the model to obtain the predicted probability values.

After examining these predicted probabilities, a threshold of 0.735 was selected, enabling the conversion of these probabilities into binary class labels (where 0 represents AAS and 1 represents APW). Interestingly, the model not only identified the AAS and APW states but also detected the SPPW state, categorizing it in the same class as AAS shown in Fig. 9(a). To delineate the boundaries between AAS-APW and APW-SPPW, we employed the Sobel edge detection algorithm [58]. The boundary data obtained from the Sobel filter is scaled to match the input data's format, and then the linear fit is taken for both boundaries separately Fig. 9(b). The regression

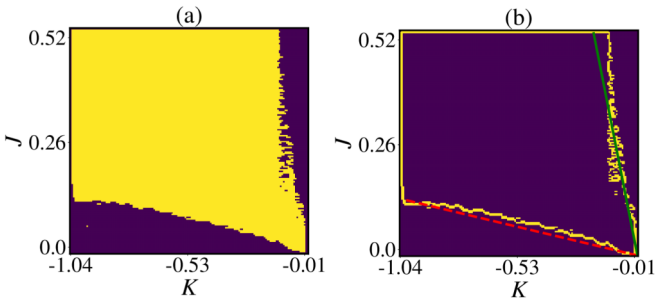

FIG. 9. JK plane as U-Net predicted labels: (a) binary predicted labels with APW region (yellow) and AAS, SPPW (deep purple); (b) boundaries identified with Sobel filter, with red dashed line representing the AAS-APW boundary and green solid line representing the APW-SPPW boundary.

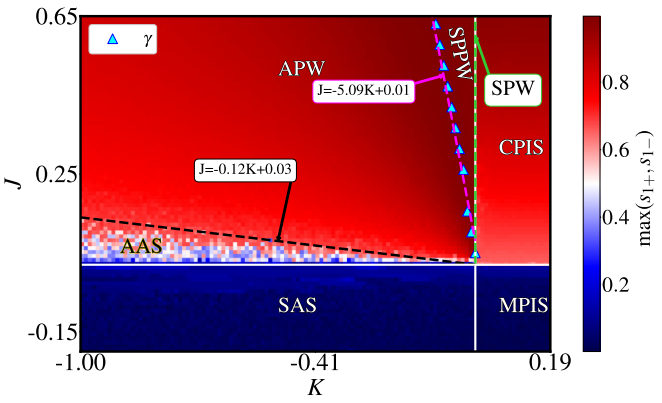

FIG. 10. JK plane of $\max(s_{1+}, s_{1-})$ shows the existence of various states corresponding to different parameter values: blue markers represent the numerical boundary of SPPW calculated from γ; the black and magenta dashed lines are the critical lines of AAS and SPPW, respectively, estimated by U-Net; the yellow solid line at $K = 0$ and $J > 0$ shows the existence of SPW; and the black and magenta dashed lines show the U-Net–predicted boundaries of AAS and SPPW, respectively. At $J = 0$ and $K = 0$, represented by white lines, the SAS and π states lose their stability. This loss of stability for the SAS state is derived from the order parameter, and for the π state it is substantiated through analytical verification.

analysis of boundary data revealed the stability boundary of AAS as $J = -0.12K + 0.003$ and SPPW as $J = -5.092K + 0.014$; the SPPW's U-Net predicted boundary is in good agreement with the boundary predicted by the order parameter γ, as seen in Fig. 10. To emphasize the effect of second-order harmonics, the dynamics of swarmalators without the harmonic term in the phase interaction are presented in Appendix C.

V. CONCLUSION

In this study we investigated the impact of second-order harmonics, particularly setting $h = 2$, introduced through the phase interaction function, on swarmalators' dynamical states, building on the findings of previous study [19]. Our findings indicate that second-order harmonics lead to clustering states such as the clustered π state (CPIS) and mixed π state (MPIS), especially when the phase coupling strength K is positive. We analytically confirmed the stability of these π states, identifying the eigenvalue $\lambda = \frac{-2K}{d}$ as key to their stability. Contrary to earlier observations, the domain of the static async state is now restricted to conditions where both J and K are unfavorable. This shift contrasts with the previously established stability of static async states at $K = -1.2J$. Furthermore, introducing second-order harmonics significantly changes the dynamics within the JK parameter plane, affecting the parameter regions of various dynamical states. One such is the emergence of an active async state, relevant to biological phenomena such as insect swarming [59] and bacterial motility [60], which occupies a transitional region between the static async state and the active phase wave state. We employed U-Net, a convolutional neural network, to identify stability boundaries between AAS, APW, and SPPW states. The determined boundaries for AAS and SPPW

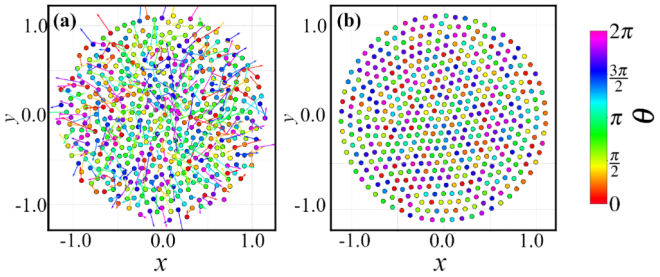

FIG. 11. Swarmalators with nonzero natural frequency. (a) The active asynchronous state at $J = 1.0$ and $K = -0.75$, which occurs throughout the parameter space where $K < 0$. The arrows show the direction of movement of the swarmalator at time t, indicating it is an active state. (b) Static asynchronous state for $J = 0.5$ and $K = 0.5$, emerging in the domain where $K > 0$.

are $J = -0.12K + 0.03$ and $J = -5.092K + 0.014$, respectively, and SPPW's boundary closely matches the numerical boundary from the order parameter γ. Our findings highlight the utility of CNN's advanced image segmentation capability in boundary estimation for dynamical systems. Immediate future research might focus on the effects of external forcing terms and second-order harmonics on various states of the swarmalators and explore potential control methods for desynchronization states such as AAS, SAS, etc.

ACKNOWLEDGMENTS

The work of R.G. and V.K.C. forms part of a research project sponsored by SERB-DST-CRG Project Grant No. C.R.G./2023/003505. R.G. and V.K.C. thanks DST, New Delhi, for computational facilities under the DST-FIST programme (Grant No. SR/FST/PS-1/2020/135) to the Department of Physics.

APPENDIX

1. Swarmalators with unimodal natural frequencies

We introduced heterogeneity to the natural frequencies by distributing the ω_i from a unimodal Cauchy distribution. This inclusion of heterogeneity led to the observation that the swarmalators exhibit only two stable configurations, as shown in Fig. 11.

2. Stability of π states

In this section we analyze the stability of π states. To sufficiently capture the essence of their collective behavior, focusing on the phase dynamics of the swarmalators is enough. The equations that describe the reduced system obtained from Eq. (4) are given as follows:

$$\dot{\theta}_1 = \frac{K}{2d}\sin\left[2(\theta_2 - \theta_1)\right], \tag{A1}$$

$$\dot{\theta}_2 = \frac{K}{2d}\sin\left[2(\theta_1 - \theta_2)\right], \tag{A2}$$

where $d = \sqrt{(x_2 - x_1)^2 + (y_2 - y_1)^2}$ represents the Euclidean distance between the two swarmalators. When the system is evaluated at the stable fixed point, we find the steady states as $\theta_1 = \psi$ and $\theta_2 = \psi + \pi$, with $h = 2$. Following this, the Jacobian matrix is calculated as follows:

$$J = \begin{pmatrix} -\frac{K}{d} & \frac{K}{d} \\ \frac{K}{d} & -\frac{K}{d} \end{pmatrix}. \tag{A3}$$

Upon determining the eigenvalues of the Jacobian J, we find that $\lambda = \frac{-2K}{d}$. This result underscores the stability of the π state for $K > 0$, which aligns with the outcomes of our numerical simulations.

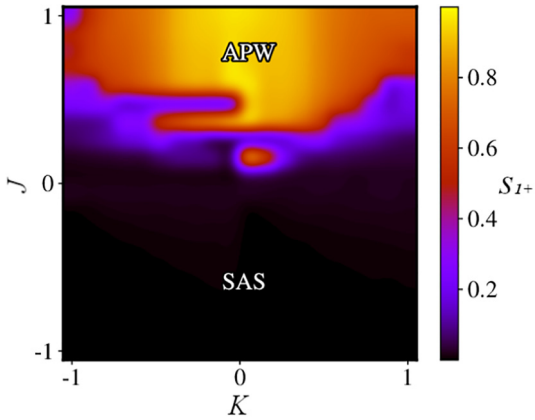

FIG. 12. J vs K plot demonstrating the absence of harmonic phase interaction through the order parameter S_{1+}.

3. Swarmalators without harmonical phase interaction

To contrast the effects of second-order harmonic phase interactions in swarmalators, we set τ_{att} in Eq. (2) to unity. This simplifies the JK parameter space to only two possible states: active phase wave (APW) and static asynchronous state (SAS). The parameter space for this case is depicted in Fig. 12.

[1] A. T. Winfree, J. Theor. Biol. **16**, 15 (1967).
[2] F. A. Rodrigues, T. K. DM. Peron, P. Ji, and J. Kurths, Phys. Rep. **610**, 1 (2016).
[3] A. E. Motter, S. A. Myers, M. Anghel, and T. Nishikawa, Nat. Phys. **9**, 191 (2013).
[4] F. Dörfler and F. Bullo, SIAM J. Control Optim. **50**, 1616 (2012).
[5] D. C. Michaels, E. P. Matyas, and J. Jalife, Circ. Res. **61**, 704 (1987).
[6] I. Aihara, H. Kitahata, K. Yoshikawa, and K. Aihara, Artif. Life Rob. **12**, 29 (2008).
[7] J. Buck, Q. Rev. Biol. **63**, 265 (1988).
[8] Z. Néda, E. Ravasz, T. Vicsek, Y. Brechet, and A.-L. Barabaási, Phys. Rev. E **61**, 6987 (2000).

[9] Y. Ma, E. W. M. Lee, M. Shi, and R. K. K. Yuen, Nat. Hum. Behav. **5**, 447 (2021).
[10] T. Vicsek, A. Czirók, E. Ben-Jacob, I. Cohen, and O. Shochet, Phys. Rev. Lett. **75**, 1226 (1995).
[11] N. Fujiwara, J. Kurths, and A. Díaz-Guilera, Phys. Rev. E **83**, 025101 (2011).
[12] K. Uriu, S. Ares, A. C. Oates, and L. G. Morelli, Phys. Rev. E **87**, 032911 (2013).
[13] J. Buhl, D. J. Sumpter, I. D. Couzin, J. J. Hale, E. Despland, E. R. Miller, and S. J. Simpson, Science **312**, 1402 (2006).
[14] I. Couzin, Nature (London) **445**, 715 (2007).
[15] J. E. Herbert-Read, J. Exp. Biol. **219**, 2971 (2016).
[16] I. D. Couzin, Curr. Biol. **28**, R976 (2018).
[17] F. Ducatelle, G. A. Di Caro, C. Pinciroli, and L. M. Gambardella, Swarm Intell. **5**, 73 (2011).
[18] M. Abdelkader, S. Güler, H. Jaleel, and J. S. Shamma, Curr. Rob. Rep. **2**, 309 (2021).
[19] K. P. O'Keeffe, H. Hong, and S. H. Strogatz, Nat. Commun. **8**, 1 (2017).
[20] A. Duggento, S. Petkoski, T. Stankovski, and N. Toschi, Front. Comput. Neurosci. **16**, 846189 (2022).
[21] K. Ota, I. Aihara, and T. Aoyagi, R. Soc. Open Sci. **7**, 191693 (2020).
[22] A. Hrabec, V. Krizakova, S. Pizzini, J. Sampaio, A. Thiaville, S. Rohart, and J. Vogel, Phys. Rev. Lett. **120**, 227204 (2018).
[23] A. Barcis and C. Bettstetter, IEEE Access **8**, 218752 (2020).
[24] M. Belovs, R. Livanovics, and A. Cebers, Phys. Rev. E **96**, 042408 (2017).
[25] J. Yan, M. Bloom, S. C. Bae, E. Luijten, and S. Granick, Nature (London) **491**, 578 (2012).
[26] D. Tanaka, Phys. Rev. Lett. **99**, 134103 (2007).
[27] M. Iwasa and D. Tanaka, Phys. Rev. E **81**, 066214 (2010)
[28] K. P. O'Keeffe, J. H. M. Evers, and T. Kolokolnikov, Phys. Rev. E **98**, 022203 (2018).
[29] K. O'Keeffe, S. Ceron, and K. Petersen, Phys. Rev. E **105**, 014211 (2022).
[30] F. Jiménez-Morales, Phys. Rev. E **101**, 062202 (2020).
[31] S. Ceron, K. O'Keeffe, and K. Petersen, Nat. Commun. **14**, 940 (2023).
[32] H. Hong, Chaos **28**, 103112 (2018).
[33] H. Hong, K. Yeo, and H. K. Lee, Phys. Rev. E **104**, 044214 (2021).
[34] G. K. Sar, S. N. Chowdhury, M. Perc, and D. Ghosh, New J. Phys. **24**, 043004 (2022).
[35] H. K. Lee, K. Yeo, and H. Hong, Chaos **31**, 033134 (2021).
[36] S. Ghosh, G. K. Sar, S. Majhi, and D. Ghosh, Phys. Rev. E **108**, 034217 (2023).
[37] L. D. Smith, arXiv:2310.01785.
[38] P. S. Skardal, E. Ott, and J. G. Restrepo, Phys. Rev. E **84**, 036208 (2011).
[39] G. B. Ermentrout and N. Kopell, J. Math. Biol. **29**, 195 (1991).
[40] I. Z. Kiss, Y. Zhai, and J. L. Hudson, Phys. Rev. Lett. **94**, 248301 (2005).
[41] J. Pathak, Z. Lu, B. Hunt, M. Girvan, and E. Ott, Chaos **27**, 121102 (2017).
[42] J. Pathak, B. Hunt, M. Girvan, Z. Lu, and E. Ott, Phys. Rev. Lett. **120**, 024102 (2018).
[43] J. Pathak, A. Wikner, R. Fussell, S. Chandra, B. R. Hunt, M. Girvan, and E. Ott, Chaos **28**, 041101 (2018).
[44] W. Hu, R. R. P. Singh, and R. T. Scalettar, Phys. Rev. E **95**, 062122 (2017).
[45] G. K. Sar and D. Ghosh, Europhys. Lett. **139**, 53001 (2022).
[46] S. Yoon, K. P. O'Keeffe, J. F. F. Mendes, and A. V. Goltsev, Phys. Rev. Lett. **129**, 208002 (2022).
[47] J. U. F. Lizárraga and M. A. M. De Aguiar, Phys. Rev. E. **108**, 024212 (2023).
[48] S. J. Ling, J. Sanny, and W. Moebs, *University Physics* (OpenStax, Houston, TX, 2016), Vol. 1.
[49] S. Ansarinasab, F. Nazarimehr, F. Ghassemi, D. Ghosh, and S. Jafari, Appl. Math. Comput. **468**, 128508 (2024)
[50] X. Qu, Y. Hu, W. Cai, Y. Xu, H. Ke, G. Zhu, and Z. Huang, Phys. Rev. Res. **6**, 013054 (2024).
[51] J. Lebert, M. Mittal, and J. Christoph, Phys. Rev. E **107**, 014221 (2023).
[52] O. Ronneberger, P. Fischer, and T. Brox, in *Medical Image Computing and Computer-Assisted Intervention, MICCAI 2015*, edited by N. Navab, J. Hornegger, W. Wells, and A. Frangi, Lecture Notes in Computer Science Vol. 9351 (Springer, Cham, 2015).
[53] L. Alzubaidi, J. Zhang, A. J. Humaidi, Y. Duan, J. Santamaría, M. A. Fadhel, and L. Farhan, J. Big Data **8**, 53 (2021).
[54] H. H. Aghdam and E. J. Heravi, *Guide to Convolutional Neural Networks* (Springer, New York, 2017).
[55] A. F. Agarap, arXiv:1803.08375.
[56] Dr. A. Usha Ruby, Int. J. Adv. Trends Comput. Sci. Eng. **9**, 5393 (2020).
[57] L. Ciampiconi, A. Elwood, M. Leonardi, A. Mohamed, and A. Rozza, arXiv:2301.05579.
[58] R. Ranjan and V. Avasthi, Wireless Pers. Commun. **132**, 651 (2023).
[59] K. van der Vaart *et al.*, Sci. Adv. **5**, eaaw9305 (2019).
[60] J. Yan, H. Monaco, and J. B. Xavier, Annu. Rev. Microbiol. **73**, 293 (2019).